

RESEARCH ARTICLE | MAY 23 2022

Controlled strained layer epitaxial growth of EuTiO_3 on buffered silicon

F. Jung   ; H. Karl 

 Check for updates

J. Appl. Phys. 131, 205303 (2022)

<https://doi.org/10.1063/5.0092582>



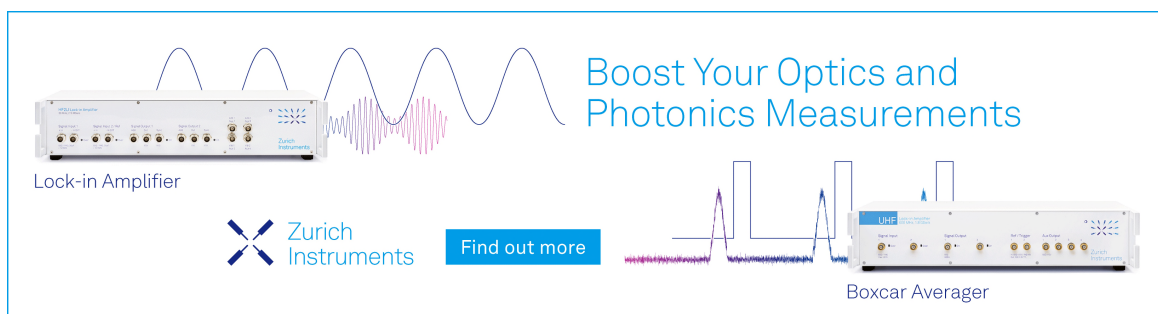
View Online




Export Citation

CrossMark

Boost Your Optics and Photonics Measurements



Lock-in Amplifier



Zurich Instruments

[Find out more](#)

Boxcar Averager

Controlled strained layer epitaxial growth of EuTiO_3 on buffered silicon

Cite as: J. Appl. Phys. 131, 205303 (2022); doi: 10.1063/5.0092582

Submitted: 23 March 2022 · Accepted: 6 May 2022 ·

Published Online: 23 May 2022



View Online



Export Citation



CrossMark

F. Jung^{a)}  and H. Karl^{b)} 

AFFILIATIONS

Institute of Physics, University of Augsburg, Universitätsstr. 1, 86159 Augsburg, Germany

^{a)}Author to whom correspondence should be addressed: florian.jung@physik.uni-augsburg.de. Present address: University of Augsburg, Universitätsstr. 1, 86159 Augsburg, Germany.

^{b)}Electronic mail: helmut.karl@physik.uni-augsburg.de

ABSTRACT

In this work, we show the epitaxial growth of (111)-oriented EuTiO_3 thin films on (001)-oriented silicon with an *in situ* grown yttria-stabilized zirconia (YSZ) buffer layer by pulsed laser deposition. X-ray diffraction measurements revealed a homogeneously strained EuTiO_3 thin film with a strain dependency on the laser fluence during the film growth. From magnetization vs temperature measurements, we confirmed that the strained EuTiO_3 films have an antiferromagnetic to ferromagnetic transition at 3.7 K, which disappeared for unstrained films. Furthermore, we used electron backscatter diffraction to analyze the columnar growth of EuTiO_3 on YSZ, which showed four in-plane orientations.

© 2022 Author(s). All article content, except where otherwise noted, is licensed under a Creative Commons Attribution (CC BY) license (<http://creativecommons.org/licenses/by/4.0/>). <https://doi.org/10.1063/5.0092582>

I. INTRODUCTION

The perovskite-type EuTiO_3 (ETO) is a well-known G-type antiferromagnetic material below a Néel temperature of $T_N = 5.3$ K.¹ It shows a variety of fascinating physical properties like a giant spin-lattice coupling,² a crossover from negative to positive magnetostriction,³ an anomalous Hall effect,⁴ a magnetocaloric effect,^{5,6} and a magnetodielectric effect.^{7,28} ETO has also drawn much attention as a potential thermoelectric oxide material due to its n-type semiconducting behavior in combination with a large Seebeck coefficient and considerably high electrical conductivity.^{8–10} The mechanical strain was found to play an important role in many of these properties, especially in the observation of a ferromagnetic transition at low temperatures in strained ETO thin films grown with pulsed laser deposition (PLD).^{11–14} Research was mainly done on polycrystalline samples and epitaxial thin films on SrTiO_3 (STO) or LaAlO_3 (LAO),^{13,15–17} whereby STO prevents a thermoelectrical characterization of the grown ETO layer due to an increase in the electrical conductivity of STO originating from oxygen vacancies, generated by reducing ETO growth conditions.^{18,19} LAO shows a structural phase transition from rhombohedral to the cubic perovskite-type structure around 534 °C,^{20,21} resulting in a potential problem for the LAO-ETO interface due to increased strain.

In this work, we present the epitaxial growth of ETO on (001)-Si substrates with a yttria-stabilized zirconia (YSZ) buffer layer. This allows the integration of the functional material ETO into silicon technology, and the electrically insulating YSZ buffer layer enables an electrical decoupling of the ETO layer from the substrate. This might, for example, allow the construction of a high-temperature oxide thin film-based thermoelectric generator (TEG) together with p-type $\text{Ca}_3\text{Co}_4\text{O}_9$, which was already proven to grow on YSZ²² epitaxially. We focus in this work on the expansion of the ETO unit cell depending on the laser fluence, as already observed in the growth of ETO on STO,¹³ and the columnar growth mechanism of ETO on YSZ in the (111) direction.

II. EXPERIMENTAL

YSZ/ETO heterostructures were grown epitaxially on (001)-Si substrates by pulsed laser deposition (PLD). The YSZ target was a commercially available sintered target with the composition $(\text{Y}_2\text{O}_3)_{0.09}(\text{ZrO}_2)_{0.91}$. The ETO-target was a single-phase EuTiO_{3-x} -target synthesized by a solid-state reaction using high purity (99.99%) Eu_2O_3 and (99.99%) TiO_2 . The two educts were stoichiometrically mixed and sintered at 1100 °C for 2 h in a reducing

12 March 2024 12:49:21

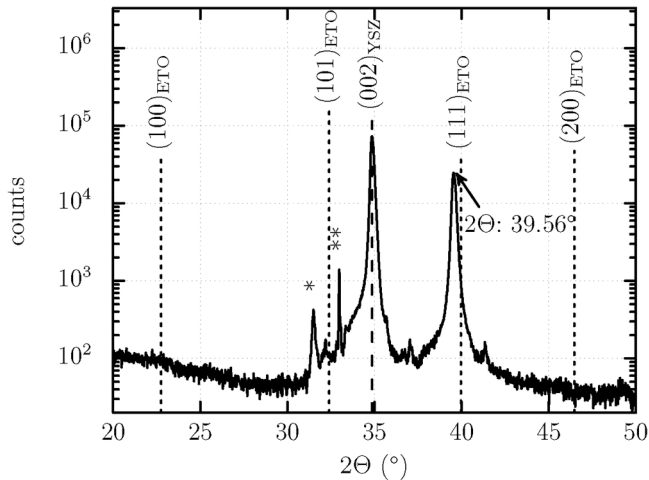


FIG. 1. XRD Θ - 2Θ scan of an ETO film grown on YSZ/Si with a laser fluence of 1.5 to 11 J cm⁻² and a substrate temperature of 830 °C. * is the Cu K β reflection of (002)_{YSZ}. ** is the forbidden (002)_{Si} reflection.

atmosphere (10% H₂, 90% Ar). The product was ball milled and sintered again under the same conditions. This procedure was repeated until the powder diffractogram showed a single-phase EuTiO₃ diffraction pattern. After the final calcination step, the powder was ball milled again, pressed in a cylindrical form with a diameter of 20 mm, and sintered a last time, leading to a high-density black target disk.

The PLD chamber is equipped with multiple targets on a holder that can move the selected target into the laser focus spot to enable *in situ* heteroepitaxial layer growth. During ablation, the target rotates for efficient and homogeneous use of the target area. The distance between the target and the substrate was 50 mm. The PLD chamber was evacuated to a base pressure of 3×10^{-6} mbar and the (001)-Si substrate heated up to a temperature of 830 °C. The growth of YSZ on (001)-Si has been optimized in previous works and can be found in the literature.^{23,24}

The YSZ layer has a thickness of 100 nm for all samples. To avoid the formation of Eu³⁺ during the ETO growth, the oxygen flow was stopped after the YSZ growth leading to a pressure of 8×10^{-6} mbar.

The target materials were ablated with a KrF excimer laser with a wavelength of 248 nm (COMPex 205 F from Coherent). To assure homogeneous irradiation of the target material, the laser beam is directed through a focusing lens, a rectangular aperture, and an imaging lens, creating a focused image of the aperture on the target surface.

For the YSZ layer, a laser fluence of 3.5 J cm⁻² and a pulse repetition rate of 3 Hz were used, the laser fluence for the ETO layer growth was varied between 1.5 and 11 J cm⁻² by a fixed laser pulse repetition rate of 2 Hz. The laser fluence was calculated by measuring the laser energy inside the deposition chamber and the dimensions of the well-defined rectangular spot on the target. X-ray diffraction (XRD) measurements were performed with a Seifert 3003 PTS equipped with a Cu-tube, and atomic force microscopy (AFM) images were taken with a Bruker Dimension Icon. A superconducting quantum interference device (SQUID) from Quantum Design was used to determine the magnetic film properties.

Scanning electron microscopy (SEM) and electron backscatter diffraction (EBSD) imaging were carried out to elucidate the crystallinity and crystal orientation of the ETO layer. They were taken with a Zeiss Merlin electron microscope equipped with a Gemini 2 electron gun and an EBSD system from Oxford NordlysNano. The multilayer system was characterized by scanning transmission electron microscopy (STEM) with a Jeol NEOARM F200. The cross-sectional sample preparation for the STEM analysis was done by cutting and gluing the sample face-to-face into a brass ring, followed by dimple-grinding and finished by Ar⁺-ion milling.

III. RESULTS AND DISCUSSION

Figure 1 shows the Θ - 2Θ diffractogram of a 200 nm thick ETO layer on YSZ/Si. The ETO layer shows a pronounced peak at $2\Theta = 39.56^\circ$, which is shifted by $\delta = 0.4^\circ$ with respect to the (111)_{ETO} diffraction peak position calculated from the bulk lattice

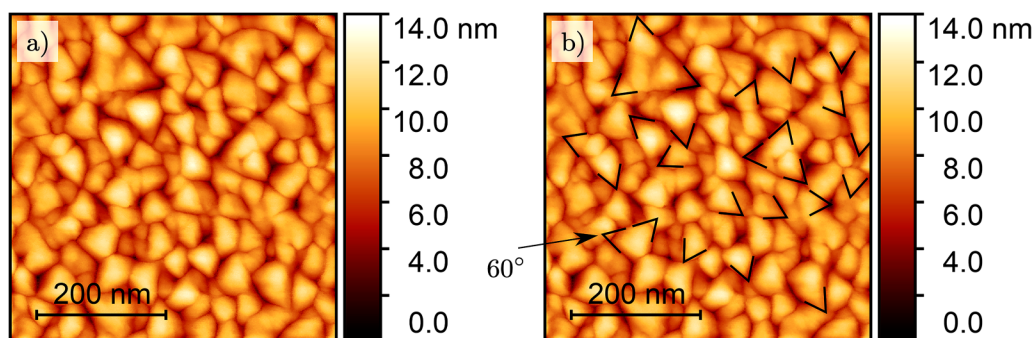


FIG. 2. AFM-scan of the 200 nm thick ETO layer on YSZ/Si from Fig. 1 with some 60°-angles marked in (b).

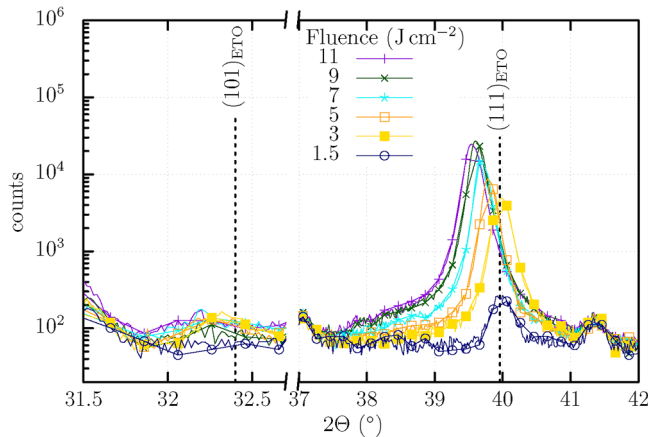


FIG. 3. XRD Θ - 2Θ scan of ETO films grown on YSZ/Si with different laser energy fluences.

parameter of 0.3905 nm^{25} of ETO. Also visible is the $(002)_{\text{YSZ}}$ reflection, and the corresponding $\text{Cu } K_{\beta}$ -peak of this reflection is marked with *. The sharp peak at $2\Theta = 32.98^\circ$ marked with ** is the forbidden $(002)_{\text{Si}}$ peak.²⁶ To analyze the ETO surface morphology, an AFM-image of the 200 nm thick ETO layer from Fig. 1 was taken, as shown in Fig. 2(a). The image shows a granular surface topography with a surface roughness of $R_{\text{RMS}} = 1.74 \text{ nm}$. The majority of the grains have a pyramidal form and triangular base area shape due to $(111)_{\text{ETO}}$ layer orientation, which is marked with 60° -angles in Fig. 2(b).

For a more detailed understanding of the shift of the $(111)_{\text{ETO}}$ diffraction peak in Fig. 1, six samples were grown in which the laser fluence was increased from sample to sample from 1.5 J cm^{-2} to 11 J cm^{-2} during ETO layer preparation. The number of pulses per ETO layer was reduced with increasing laser fluence. All other growth parameters were maintained fixed. Figure 3 shows high resolution Θ - 2Θ -scans around the diffraction angles of the $(111)_{\text{ETO}}$ and $(101)_{\text{ETO}}$ diffraction peaks. The absence of $(101)_{\text{ETO}}$ diffraction

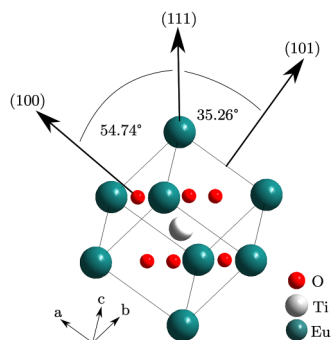


FIG. 4. Scheme of the (111) and (101) direction with respect to the (111) direction in a EuTiO_3 unit cell.

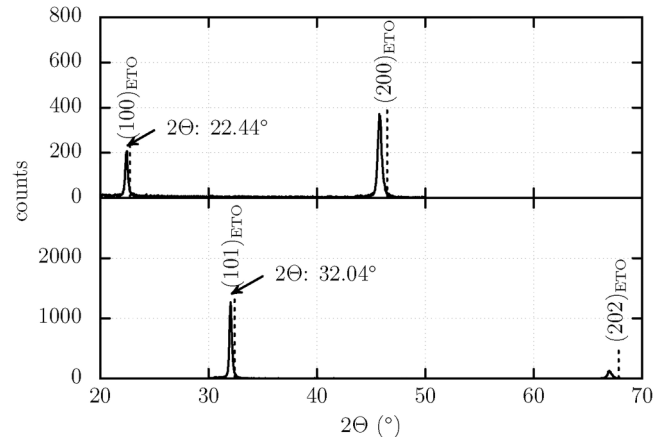


FIG. 5. XRD Θ - 2Θ scan of the ETO layer from Fig. 1 tilted by 54.74° (top) and 35.26° (bottom) along χ .

peaks proves that an entirely (111) -oriented layer of ETO was grown on YSZ.

Analogous to the growth of ETO on STO,^{13,15} ETO shows a similar out-of-plane lattice constant expansion with increasing laser fluence. The out of plane lattice constant increased from the bulk value of 0.3905 nm at 1.5 and 3 J cm^{-2} to 0.3946 nm at 11 J cm^{-2} . The variation in the diffraction peak intensity is caused by a decrease in the film thickness with decreasing laser fluence. To exclude a correlation between the ETO layer thickness and the lattice expansion, we further grew a series of samples with varying thicknesses at a constant fluence, showing no dependency of the shift with the layer thickness. To further analyze the deformation of the unit cell, we measured Θ - 2Θ -scans of the $(100)_{\text{ETO}}$ and $(101)_{\text{ETO}}$ planes of the ETO layer shown in Fig. 1. This was achieved by aligning the samples along the $(002)_{\text{Si}}$ reflection and tilting the sample by 54.74° along the χ -axis for the $(100)_{\text{ETO}}$ plane and 35.26° along χ for the $(101)_{\text{ETO}}$ plane (see Fig. 4). The Θ - 2Θ -scans are shown in Fig. 5. Analogous to the $(111)_{\text{ETO}}$ plane, both orientations show shifted peaks. Since both the $(100)_{\text{ETO}}$ and $(101)_{\text{ETO}}$ planes carry information about the in-plane lattice, the shifted peaks lead to the assumption of an isotropic expanded unit cell and to an altering of unit cell volume, which is in contrast to the uni-axial strain found along the c -axis in the growth of ETO on STO in (001) direction.¹³ The measurements of the (100) and (101) plane for the ETO-layers grown with 1.5 and 3 J cm^{-2} showed no shift of the peak from the peak position of the bulk value. The resulting strain

TABLE I. Lattice plane, peak position, lattice parameter, and strain calculated from the Θ - 2Θ -scans of the (111) , (101) , and (100) orientations.

(hkl)	2Θ ($^\circ$)	a (\AA)	Strain (%)
(111)	39.56	3.944	0.97
(101)	32.04	3.949	1.10
(100)	22.44	3.960	1.38

12 March 2024 12:49:21

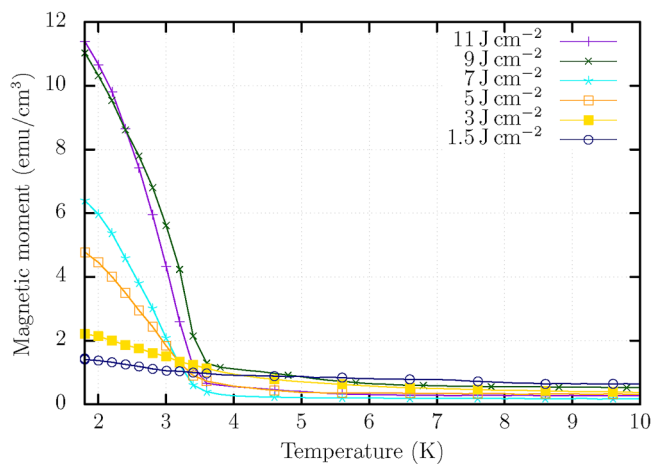


FIG. 6. Temperature dependence of the magnetic moment with varying laser energy fluences under field cooling conditions for the ETO-films.

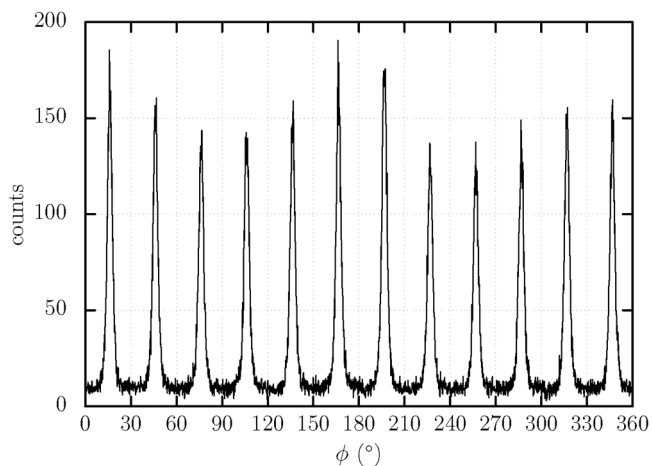


FIG. 7. XRD ϕ -scan of the (100)_{ETO}-reflection in Fig. 5.

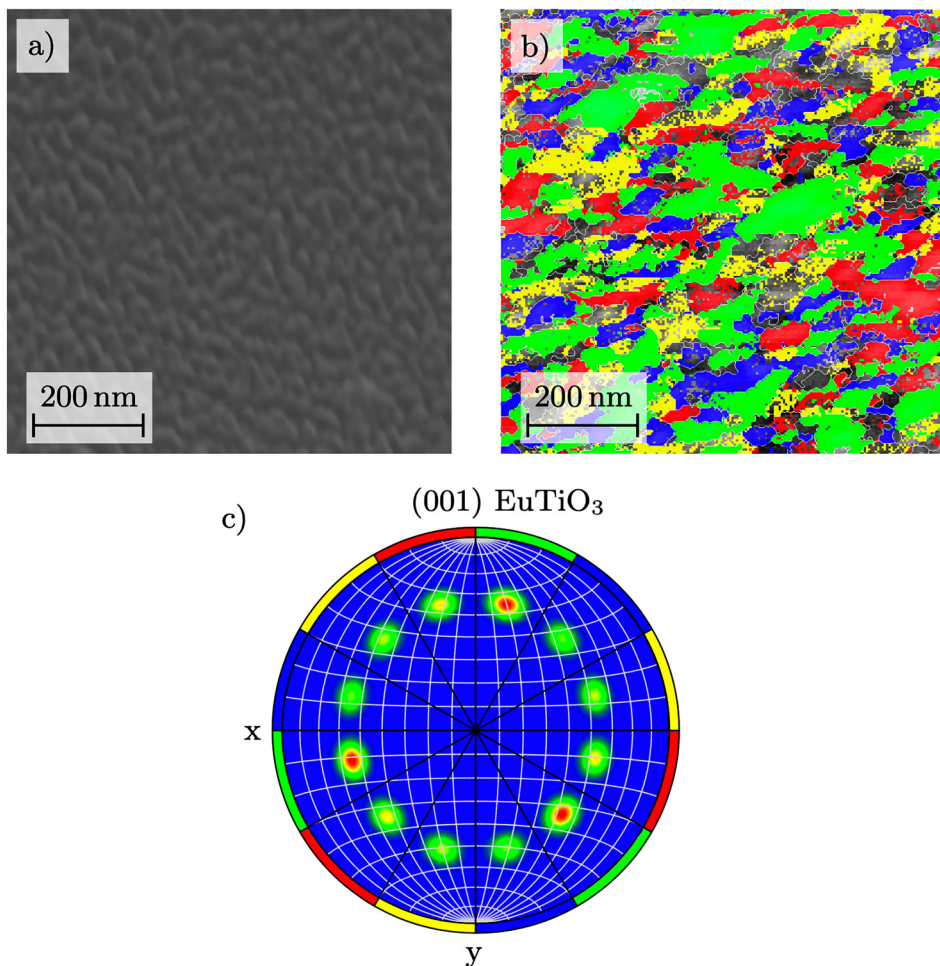


FIG. 8. (a) SEM image of the ETO layer surface revealing a slightly granular surface, (b) in-plane crystal-orientation measured by the in-plane Euler angular ϕ with band-contrast in the background. The color-code is generated by assigning each crystal orientation a color. (c) Pole figure calculated from the EBSD-mapping and color code of the orientation from (b).

12 March 2024 12:49:21

calculated in all three directions based on the XRD measurements is summarized in Table I. It was theoretically calculated by Craig and Rabe²⁷ and later on shown by several groups,^{11,13,15–17} that growth-related strain in epitaxial ETO-films show an antiferromagnetic to ferromagnetic transition below 4 K. We used this antiferromagnetic to ferromagnetic transition to further show the correlation between strain in the ETO films and the laser fluence. Figure 6 shows the temperature dependence of the magnetic moment for the sequence of samples grown with increasing laser fluences as shown in Fig. 3. All measurements were done under field cooling conditions with a magnetic field of 10 mT. The ETO-layer grown with 1.5 J cm^{-2} shows a vanishingly small magnetic moment, which would be expected from a non-strained and, therefore, antiferromagnetic ETO-layer. The ETO-layer grown with 3 J cm^{-2} shows a gradual increase in the magnetic moment below 4 K. Significant changes are visible in the ETO-layers with 5 J cm^{-2} and higher. Visual is here the antiferromagnetic to ferromagnetic transition around 3.7 K.

We further analyzed the in-plane orientation of the growth of ETO on YSZ/Si measuring the $(100)_{\text{ETO}}$ -reflection along the ϕ axis. The resulting ϕ -scan is shown in Fig. 7. The measurement shows a 12-fold symmetry around the (111) -axis with an equidistant peak distance of $\Delta\phi = 30^\circ$. The enveloping curve on the peaks shows a slight oscillation which could be the result of a non-uniform distribution of ETO in-plane orientations. The 12-fold symmetry indicates four in-plane orientations rotated by 30° , respectively.

To analyze the epitaxial relationship between YSZ and ETO, we used SEM combined with an EBSD detector. The resulting measurement is shown in Figs. 8(a) and 8(b). The SEM image in Fig. 8(a) reveals a uniform textured surface with a grain size of around 50 nm, which is in agreement with grains observed in the AFM-scan in Fig. 2. The EBSD mapping in Fig. 8(b) was generated by overlaying the bandcontrast with the local orientation from the in-plane Euler angles. Additionally, a pole figure was generated from the in-plane Euler angles, as shown in Fig. 8(c), where the coloring is done according to Fig. 8(b). The pole figure shows analogous to the ϕ -scan in Fig. 7, a 12-fold symmetry around the $(111)_{\text{ETO}}$ -axis. The pole figure and the EBSD-scan show a slightly preferred growth direction (green). Due to the small scan area, this could not represent the entire layer, although the oscillation of the enveloping curve in Fig. 7 also suggests a slightly preferred in-plane orientation of ETO. The available data do not permit final judgment on this matter.

The EBSD-scan shows mainly areas with the size of $100\text{--}200 \text{ nm}^2$ with the same orientation.

Figure 9 shows a high-resolution, unfiltered STEM image of a cross section of the ETO layer. At the bottom, a few unit cells of YSZ are visible. The brightness contrast in both layers originates from the difference in the atomic number. It represents, therefore, the location of Eu- in the upper layer and Zr-atoms in the bottom layer. The sample was orientated along the $(010)_{\text{Si}}$ -axis. Due to the sample preparation process and, especially, Ar^+ -ion milling, an amorphized layer on the ETO-layer is formed, recognizable in the top part of the image by a 10 nm thick granular layer. In the left part of the image, equidistant layers are visible with a distance of 2.282 \AA , which corresponds to the (111) lattice plane distance of ETO. On the right side, two single crystalline grains are visible in which the corresponding crystal orientations could be determined.

High-resolution STEM images with corresponding unit cell orientations are shown in the insets above. The STEM analysis supports the findings from the XRD and EBSD analyses of a growth of ETO on YSZ in (111) -orientation with in-plane rotated grains. The analysis also shows that the four different orientations have no offset in in-plane rotation concerning the YSZ layer. Together with the results from the EBSD- and ϕ -scan, the epitaxial relationship between ETO and YSZ can be summarized in Fig. 10. All four orientations have an equivalent lattice mismatch $\frac{a_{\text{YSZ}} - a_{\text{ETO}}}{a_{\text{YSZ}}}$ in both directions of 6.53% and -7.93% . The lattice mismatch in Fig. 10 applies only for the unit cells where the lattice mismatch is marked in gray. All neighboring unit cells increase the lattice mismatch with increasing distance from this initial ETO unit cell. The lattice mismatch leads to fast relaxation within a few unit cells in the out-of-plane direction, as seen in the STEM image and XRD measurements. In the in-plane direction, the mismatch is most likely

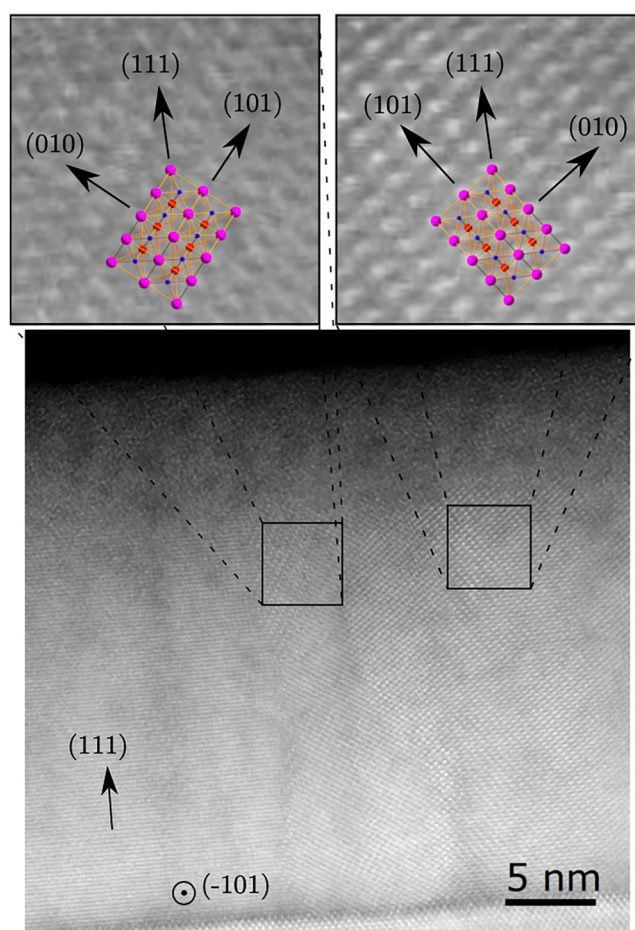


FIG. 9. STEM image of the ETO-layer and a few unit cells of YSZ at the bottom. The insets show the magnified rectangular areas and the corresponding crystal orientations with the overlaid unit cells of ETO and crystal axes with miller indices.

12 March 2024 12:49:21

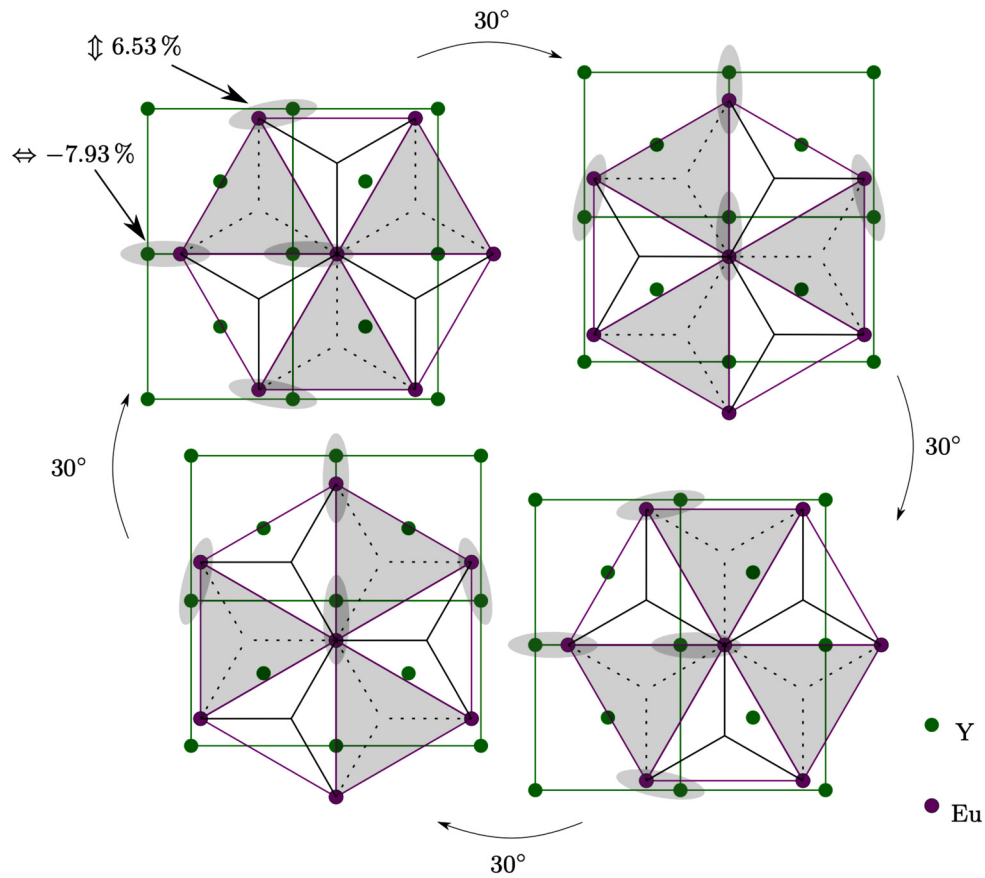


FIG. 10. Scheme of the unit cell arrangement of the EuO-sublattice and the YSZ-surface. The lattice mismatch is equivalent in all four arrangements. The gray shaded areas of the EuO-sublattice go into the plane of the drawing and the white areas out of the plane.

12 March 2024 12:49:21

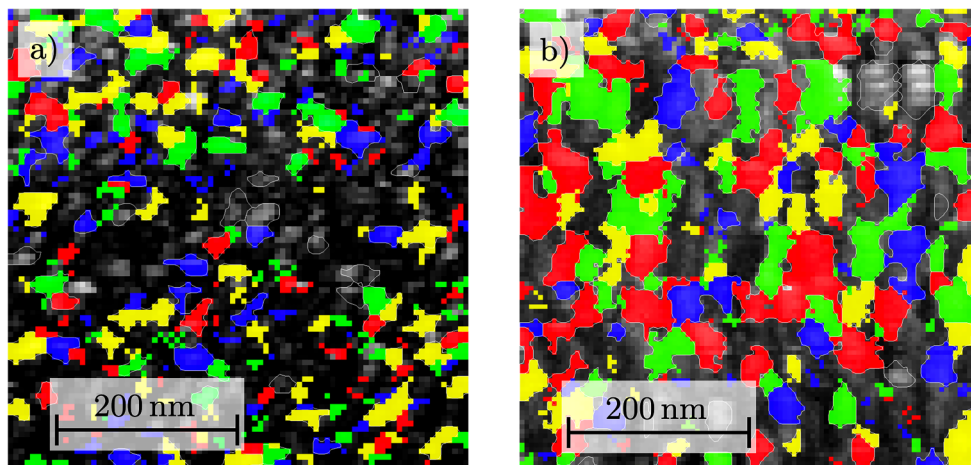


FIG. 11. EBSD-scan of the sample surface of a 50 nm (a) and 100 nm (b) thick layer of ETO grown on YSZ. For both images, the local orientation from the in-plane Euler angle was layed on top of the bandcontrast.

the reason for the formation of grains in the ETO film. We further analyzed ETO grain size dependency on the layer thickness. This was achieved by comparing the EBSD-scans of three different ETO layer thicknesses of 50, 100, and 200 nm. The EBSD-scans of 50 and 200 nm thick ETO layers are shown in Figs. 11(a) and 11(b). The 50 nm thick layer shows grain diameters of 10–50 nm and a rather homogeneous distribution of different orientations. The EBSD-scan in Fig. 11(b) with an ETO layer thickness of 100 nm shows much bigger grain diameters of 50–100 nm and also no significantly preferred orientation. The EBSD-scan of the 200 nm thick ETO layer is shown in Fig. 8(b), and it shows the largest grain diameters with 100–200 nm. This columnar growth with an increase in grain surface with increasing columnar length can also be seen in the STEM image as shown in Fig. 9.

IV. CONCLUSION

We have demonstrated the successful growth of ETO on a (001)-orientated silicon substrate with a YSZ buffer layer by PLD. ETO grows epitaxially on YSZ in the (111)-direction with a 12-fold in-plane rotational symmetry. We could identify the four different in-plane orientations via EBSD-scans and show a columnar growth of different orientations with an increase in the grain surface with increasing columnar length. With XRD and SQUID measurements, we could prove that it is possible to control a homogeneous strain in ETO with the laser fluence during the ablation process. In contrast to the uni-axial strain found along the c-axis in the growth of ETO on STO in the (001) direction,¹³ ETO on YSZ shows an almost homogeneous strain along the (111)-, (101)-, and (100)-axes.

The growth of ETO on silicon via PLD allows the integration of the functional material ETO into silicon technology. It presents a tool to control a homogeneous strain in the ETO layer and the magnetic properties.

ACKNOWLEDGMENTS

We would like to acknowledge the support from Dr. Aladin Ullrich who contributed the STEM image presented in this work.

SUPPLEMENTARY MATERIAL

See the [supplementary material](#) for the three Euler angles used to determine the crystal orientation in Fig. 8 as well as a more detailed description of the EBSD measurement.

AUTHOR DECLARATIONS

Conflict of Interest

The authors have no conflicts to disclose.

DATA AVAILABILITY

The data that support the findings of this study are available from the corresponding author upon reasonable request.

REFERENCES

¹T. R. McGuire, M. W. Shafer, R. J. Joenk, H. A. Alperin, and S. J. Pickart, "Magnetic structure of EuTiO₃," *J. Appl. Phys.* **37**, 981–982 (1966).

²T. Birol and C. J. Fennie, "Origin of giant spin-lattice coupling and the suppression of ferroelectricity in EuTiO₃ from first principles," *Phys. Rev. B* **88**, 094103 (2013).

³P. G. Reuvekamp, R. K. Kremer, J. Köhler, and A. Bussmann-Holder, "Spin-lattice coupling induced crossover from negative to positive magnetostriction in EuTiO₃," *Phys. Rev. B* **90**, 094420 (2014).

⁴K. S. Takahashi, H. Ishizuka, T. Murata, Q. Y. Wang, Y. Tokura, N. Nagaosa, and M. Kawasaki, "Anomalous Hall effect derived from multiple Weyl nodes in high-mobility EuTiO₃ films," *Sci. Adv.* **4**, eaar7880 (2018).

⁵R. Das, R. Prabhu, N. Venkataramani, S. Prasad, L. Li, M.-H. Phan, V. Keppens, D. Mandrus, and H. Srikanth, "Giant low-field magnetocaloric effect and refrigerant capacity in reduced dimensionality EuTiO₃ multiferroics," *J. Alloys Compd.* **850**, 156819 (2021).

⁶A. Midya, P. Mandal, K. Rubi, R. Chen, J.-S. Wang, R. Mahendiran, G. Lorusso, and M. Evangelisti, "Large adiabatic temperature and magnetic entropy changes in EuTiO₃," *Phys. Rev. B* **93**, 094422 (2016).

⁷T. Katsufuji and H. Takagi, "Coupling between magnetism and dielectric properties in quantum paraelectric EuTiO₃," *Phys. Rev. B* **64**, 147 (2001).

⁸X. Xiao, M. Widenmeyer, K. Küster, M. Scavini, S. Checchia, C. Castellano, D. Ma, S. Yoon, W. Xie, U. Starke, K. Zakharchuk, A. Kovalevsky, and A. Weidenkaff, "A squeeze on the perovskite structure improves the thermoelectric performance of europium calcium titanates," *Mater. Today Phys.* **7**, 96–105 (2018).

⁹L. Sagarna, A. Shkabko, S. Populoh, L. Karvonen, and A. Weidenkaff, "Electronic structure and thermoelectric properties of nanostructured EuTi_{1-x}Nb_xO_{3-δ} (x = 0.00; 0.02)," *Appl. Phys. Lett.* **101**, 033908 (2012).

¹⁰L. Sagarna, K. Z. Rushchanskii, A. Maegli, S. Yoon, S. Populoh, A. Shkabko, S. Pokrant, M. Ležaić, R. Waser, and A. Weidenkaff, "Structure and thermoelectric properties of EuTi(O, N)_{3±δ}," *J. Appl. Phys.* **114**, 033701 (2013).

¹¹K. Fujita, N. Wakasugi, S. Murai, Y. Zong, and K. Tanaka, "High-quality anti-ferromagnetic EuTiO₃ epitaxial thin films on SrTiO₃ prepared by pulsed laser deposition and postannealing," *Appl. Phys. Lett.* **94**, 062512 (2009).

¹²Z.-G. Li, R. Zhao, W. Li, H. Wang, H. Yang, and Y.-L. Song, "Strain dependent ultrafast carrier dynamics in EuTiO₃ films," *Appl. Phys. Lett.* **105**, 162904 (2014).

¹³R. Zhao, Y. Ji, C. Yang, W. Li, Y. Zhu, W. Zhang, H. Lu, Y. Jiang, G. Liu, J. Hong, H. Wang, and H. Yang, "Origin of unexpected lattice expansion and ferromagnetism in epitaxial EuTiO_{3-δ} thin films," *Ceram. Int.* **46**, 19990–19995 (2020).

¹⁴K. Tanaka, K. Fujita, Y. Maruyama, Y. Kususe, H. Murakami, H. Akamatsu, and S. Murai, "Effect of substrate strain and interface on magnetic properties of EuTiO₃ thin film," *MRS Proc.* **1454**, 149–159 (2012).

¹⁵Y. Lin, E.-M. Choi, P. Lu, X. Sun, R. Wu, C. Yun, B. Zhu, H. Wang, W. Li, T. Maity, and J. MacManus-Driscoll, "Vertical strain-driven antiferromagnetic to ferromagnetic phase transition in EuTiO₃ nanocomposite thin films," *ACS Appl. Mater. Interfaces* **12**, 8513–8521 (2020).

¹⁶K. Tanaka, K. Fujita, Y. Maruyama, Y. Kususe, H. Murakami, H. Akamatsu, Y. Zong, and S. Murai, "Ferromagnetism induced by lattice volume expansion and amorphization in EuTiO₃ thin films," *J. Mater. Res.* **28**, 1031–1041 (2013).

¹⁷J. H. Lee, L. Fang, E. Barnes, X. Ke, Y. Jung, L. Kourkoutis, J.-W. Kim, P. Ryan, T. Heeg, M. Roeckerath, V. Goian, M. Bernhagen, R. Uecker, P. Hammel, K. Rabe, S. Kamba, J. Schubert, J. Freeland, D. Muller, and D. Schlom, "A strong ferroelectric ferromagnet created by means of spin-lattice coupling," *Nature* **476**, 114 (2011).

¹⁸H. Trabelsi, M. Bejar, E. Dhahri, M. Sajieddine, K. Khirouni, R. Prezas, B. M. G. Melo, M. A. Valente, and M. P. F. Graca, "Effect of oxygen vacancies on SrTiO₃ electrical properties," *J. Alloys Compd.* **723**, 894–903 (2017).

¹⁹P. P. Balakrishnan, M. J. Veit, U. S. Alaán, M. T. Gray, and Y. Suzuki, "Metallicity in SrTiO₃ substrates induced by pulsed laser deposition," *APL Mater.* **7**, 011102 (2019).

²⁰S. A. Hayward, S. A. T. Redfern, and E. K. H. Salje, "Order parameter saturation in LaAlO₃," *J. Phys.: Condens. Matter* **14**, 10131–10144 (2002).

- ²¹S. Bueble, K. Knorr, E. Brecht, and W. W. Schmahl, "Influence of the ferroelastic twin domain structure on the 100 surface morphology of LaAlO₃ HTSC substrates," *Surf. Sci.* **400**, 345–355 (1998).
- ²²A. Griebner, T. Kraus, O. Klein, and H. Karl, "Low-resistance electrical contact between epitaxially grown thermoelectric oxide material (Ca₂CoO₃)_{0.62}CoO₂ and iridium," *Thin Solid Films* **717**, 138420 (2021).
- ²³H. Karl, J. Hartmann, and B. Stritzker, "In-plane lattice constant relaxation during laser ablation of YBCO and yttria-stabilized zirconia," *Thin Solid Films* **241**, 84–87 (1994), papers presented at the European Materials Research Society 1993 Spring Conference, Symposium C: Ion Beam, Plasma, Laser and Thermally-Stimulated Deposition Processes, Strasbourg, France, May 4–7, 1993.
- ²⁴M. Fischer, S. Gsell, M. Schreck, R. Brescia, and B. Stritzker, "Preparation of 4-inch Ir/YSZ/Si(001) substrates for the large-area deposition of single-crystal diamond," *Diamond Relat. Mater.* **17**, 1035–1038 (2008), Proceedings of Diamond 2007, the 18th European Conference on Diamond, Diamond-Like Materials, Carbon Nanotubes, Nitrides and Silicon Carbide.
- ²⁵J. Brous, I. Fankuchen, and E. Banks, "Rare earth titanates with a perovskite structure," *Acta Crystallogr.* **6**, 67–70 (1953).
- ²⁶P. Zaumseil, "High-resolution characterization of the forbidden Si 200 and Si 222 reflections," *J. Appl. Crystallogr.* **48**, 528–532 (2015).
- ²⁷C. Fennie and K. Rabe, "Magnetic and electric phase control in epitaxial EuTiO₃ from first principles," *Phys. Rev. Lett.* **97**, 128 (2006).
- ²⁸S. Kamba, D. Nuzhnyy, P. Vanek, M. Savinov, K. Knizek, Z.-Z. Shen, E. Šantavá, K. Maca, M. Sadowski, and J. Petzelt, "Magnetodielectric effect and optic soft mode behaviour in quantum paraelectric EuTiO₃ ceramics," *Europhys. Lett.* **80**, 27002 (2007).